J. Fluid Mech. (1981), *vol.* 113, *pp.* 299-313
Printed in Great Britain

Development of flow field when a symmetrical underexpanded sonic jet impinges on a flat plate

By J. IWAMOTO† AND B. E. L. DECKKER

Mechanical Engineering Department, University of Saskatchewan, Saskatoon, Saskatchewan, Canada, S7N OWO

(Received 27 March 1980 and in revised form 20 April 1981)

A differencing scheme known as the 'Fluid-in-Cell' method has been used in the numerical simulation of a choked jet of air impinging on a flat plate. Before sonic conditions are applied at the nozzle exit, the field of interest is at rest at the ambient pressure and temperature. The instantaneous application of sonic conditions at the nozzle exit is tantamount to the sudden appearance of a normal shock wave whose strength is determined by the experimental conditions.

The results of the simulation describe the decay of the initial shock wave and its reflection at the plate; the formation of a second shock wave and its merging with the reflected shock giving rise to a detached shock wave which oscillates; and the growth and subsequent motion of a toroidal vortex that is generated between this shock wave and the plate. The results show clearly how the flow field which has been observed in physical experiments under stable operating conditions is developed.

1. Introduction

An underexpanded sonic jet is obtained when a gas is allowed to expand through a convergent nozzle in which the ratio of the stagnation pressure p_t to the ambient pressure p_0 is higher than the critical pressure ratio (1·893 in case of air). The flow velocity is sonic at the nozzle exit plane, and downstream where the velocity becomes supersonic, the pressure decreases below that of the ambient medium. If a flat plate is placed normal to the jet axis at a certain distance from the nozzle, a detached shock wave is formed in front of the plate and a toroidal vortex is also formed between the shock wave and the plate. It is known that the shock wave oscillates along the jet axis and that the formation of the vortex is periodic.

The presence of a 'stand-off' shock wave ahead of a blunt body was first briefly described by Thompson (1964) in connection with work on resonance tubes. He found that the flow in front of a plugged tube was unsteady when an underexpanded sonic jet was directed against it but when a uniform supersonic jet was used the flow was stable. Similar observations have been made by Henderson (1966) and by Donaldson & Snedeker (1971).

Moerch (1964) proposed a theory for the oscillation of the shock wave under stable operating conditions based on the method of small perturbations which gave results that were in reasonable agreement with experimental oscillation frequencies. How-

† Permanent Address: Tokyo Denki University, 2–2 Nishiki-Cho, Kanda, Chiyoda-Ku Tokyo, Japan.

ever, his theory was one-dimensional in the sense that he considered conditions only on the axis joining the nozzle to the plate.

Kukita (1975) studied the problem experimentally using schlieren optics to reveal the oscillating shock wave and the flow pattern in the vicinity of an infinite plate. The detailed structure of the flow field could not be described quantitatively from the schlieren photographs as the resolution was limited by the sensitivity of the optical system and by the photogrammetric technique.

Generally, experimental determination of details of the flow field in this and in related problems (Hartmann 1931; Iwamoto & Deckker 1979) is limited by the scale of the experiment and by the measuring techniques that can be employed, since not only is the flow non-uniform and unsteady but it is also of the mixed type in which supersonic and subsonic regions coexist.

A finite-difference scheme known as the 'Fluid-in-Cell' (FLIC) method has been used to obtain details of the flow field starting from the instant that sonic conditions are applied at the nozzle exit. This difference scheme has been successfully applied to time-dependent compressible flows (Deckker & Yang 1975; Deckker 1979). Truncation errors introduced by numerical approximations and the use of an artificial viscosity, required for computational stability, act to some extent like a natural viscosity and give results which approximate closely to the real flow.

2. Fluid-in-cell method

The method is fully described elsewhere (Gentry, Martin & Daly 1966) and only the main features of the scheme are discussed here.

Finite-difference formulae are obtained from the laws of conservation involving the fluxes of mass, momentum and energy. For time-dependent axially symmetric compressible flows these are, respectively,

$$\frac{\partial \rho}{\partial t}+\frac{1}{r}\frac{\partial \rho r v}{\partial r}+\frac{\partial \rho u}{\partial x}=0, \tag{1}$$

$$\frac{\partial \rho u}{\partial t}+\frac{\partial \rho u^2}{\partial x}+\frac{\partial \rho u v}{\partial r}+\frac{\rho u v}{r}+\frac{\partial P}{\partial x}=0, \tag{2}$$

$$\frac{\partial \rho v}{\partial t}+\frac{\partial \rho u v}{\partial x}+\frac{\partial \rho v^2}{\partial r}+\frac{\rho v^2}{r}+\frac{\partial P}{\partial r}=0, \tag{3}$$

$$\frac{\partial \rho E}{\partial t}+\frac{\partial \rho u E}{\partial x}+\frac{\partial \rho v E}{\partial r}+\frac{\rho E v}{r}+\frac{\partial P u}{\partial x}+\frac{\partial P v}{\partial r}+\frac{P v}{r}=0, \tag{4}$$

where x and r are cylindrical co-ordinates; u, v are the x and r components of velocity. The energy is defined by $E = I+\frac{1}{2}(u^2+v^2)$, where I is the specific internal energy; $P = p+q$, where p is the thermodynamic pressure and q is an artificial viscous 'pressure' which is used to smear the shock wave and allow calculations to be made at the discontinuity. The use of artificial viscosity also enhances stability in the far subsonic regions of the flow. The form of q is given by

$$q = b\rho a\frac{\partial u}{\partial x} \quad \left(\text{or } b\rho a\frac{\partial v}{\partial r}\right), \tag{5}$$

where a is the local acoustic velocity and b is an adjustable constant.

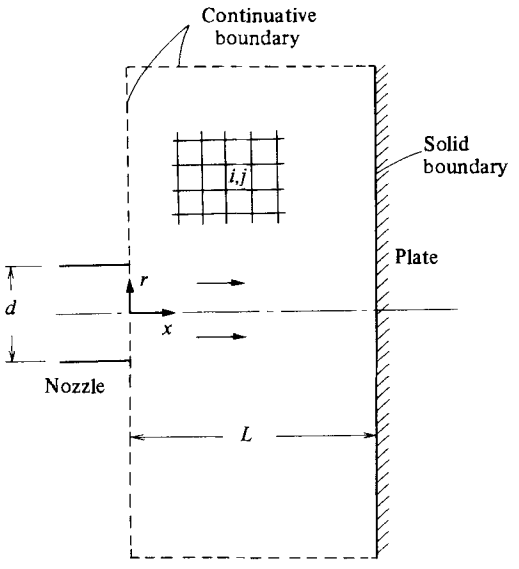

FIGURE 1. Projection of flow field on (x, r)-plane and computing mesh. $d = 8$ mm, $L = 18$ mm.

In addition to the above equations, the equation of state for the fluid has to be prescribed. For a perfect gas with constant specific heats, the equation of state is $p = (\gamma - 1)\rho I$.

The computing mesh is formed by dividing the region of interest into a finite number of cells, as shown in figure 1. Each cell is characterized by certain average values of the flow variables, such as density, pressure, specific internal energy and velocity components. Given the initial values of these variables for each cell, and with the boundary conditions prescribed, finite-difference approximations of the conservation laws provide the means whereby the cell quantities are advanced in time through a small increment Δt.

Firstly, cell pressures are calculated using the specified equation of state. The initial phase of the calculation involves the determination of provisional values of the velocities u, v and specific internal energy I, based on the assumption that the fluid mass in each cell remains fixed, that is, there is no mass flow across cell boundaries. The second step involves the calculation of transport effects, assuming that the mass which flows from cell to cell is directly proportional to the density of the donor cell (the cell from which the fluid is flowing). This method, called 'donor-cell differencing', results in good stability properties in low-velocity regions, and it eliminates the possibility of a cell emptying itself. By applying the law of conservation of mass flow across cell boundaries a new value of density for each cell at the end of a time cycle (i.e. for $t + \Delta t$) is obtained. Finally, transport of momentum and energy are calculated from the conservation laws, assuming that the mass which flows across the cell boundaries carries with it the provisional values of the velocities and the specific energy of the donor cell. From the momentum and energy determined in this manner final values of the velocities and the specific internal energy are calculated. These calculations are repeated for each time cycle.

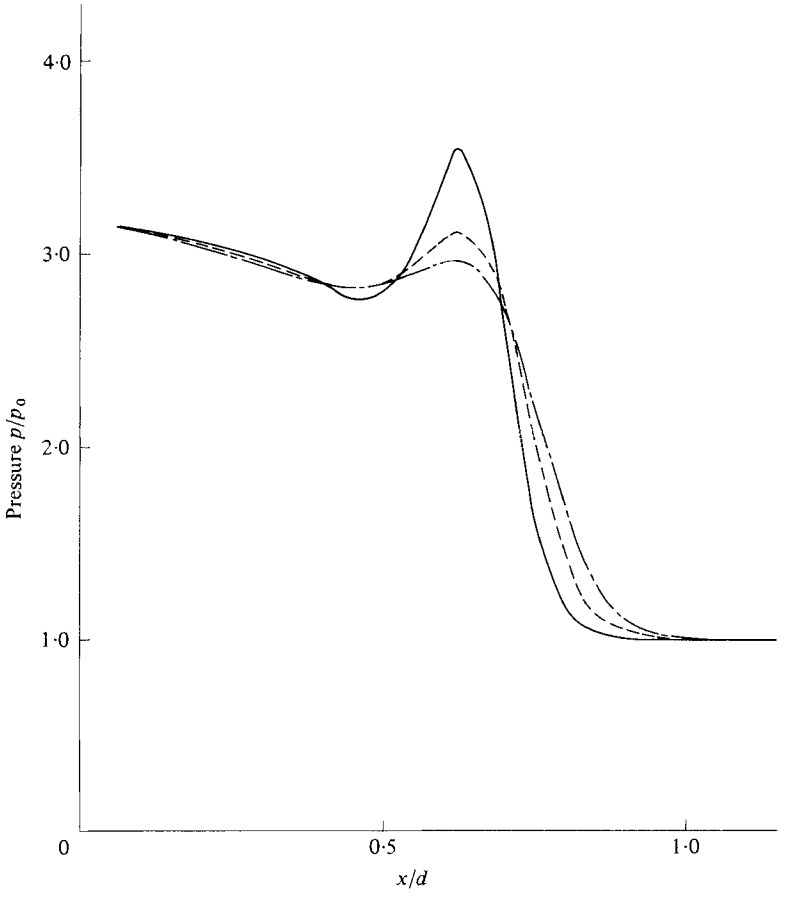

FIGURE 2. Effect of b, equation (5), on pressure distribution on axis at $\tau = 0{\cdot}45$. ——, $b = 0$; – – –, $b = 0{\cdot}3$; –· –, $b = 0{\cdot}5$.

3. Initial and boundary conditions

Figure 1 shows the projection on the x, r plane of the flow field under consideration. A volume bounded by planes containing the flat plate and nozzle exit and extending radially some distance from the axis of symmetry, that is, on either side of the line joining the centre of the nozzle to the plate, defines the extent of the flow field. It is divided by annuli whose cross-sections are the uniformly rectangular cells seen in figure 1.

Initially, every point in the field of interest is at rest at the pressure and temperature of the atmosphere. The boundary conditions are there that are no fluxes of momentum or energy across solid boundaries and the axis of symmetry, so that the velocity normal to these boundaries must be zero. At other boundaries the required condition is that normal space derivatives of the variables vanish.

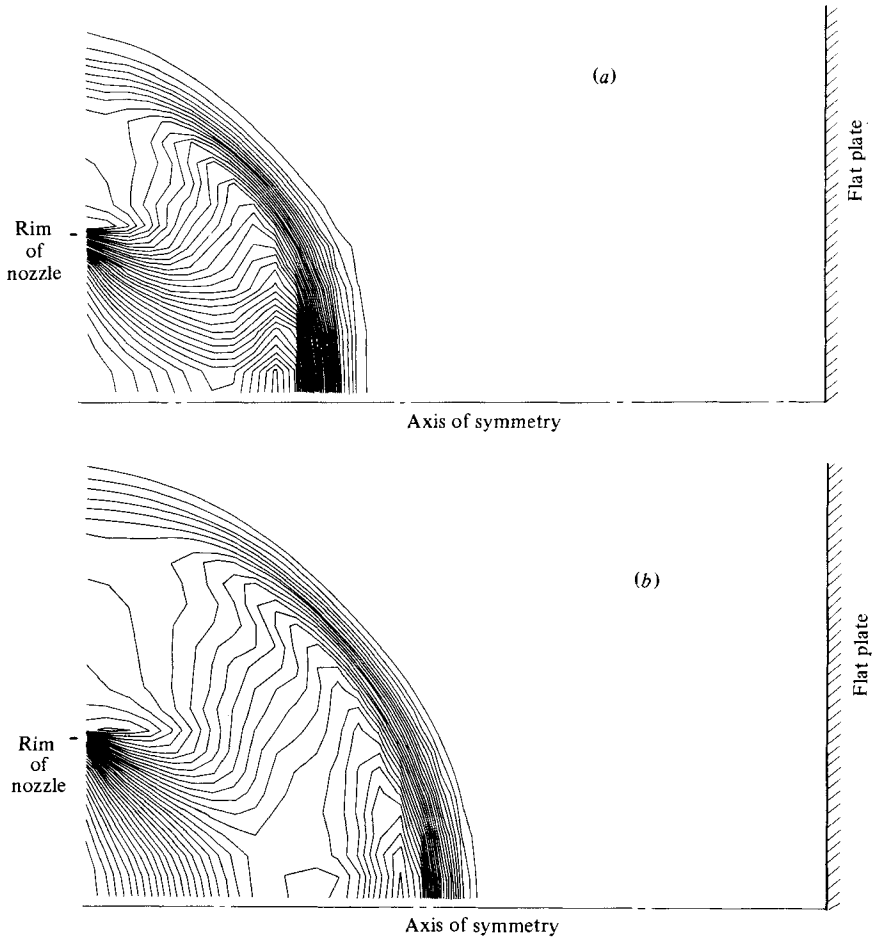

FIGURE 3. Pressure contours behind expanding shock wave: (*a*) at $\tau = 0{\cdot}446$; (*b*) at $\tau = 0{\cdot}664$.

4. Results and discussion

The diameter of the nozzle, the nozzle–plate spacing, and other physical conditions have been taken from Kukita (1975). The exit diameter of the nozzle is 8 mm and the nozzle–plate spacing 18 mm. The nozzle pressure ratio p_t/p_0 (p_t is the jet stagnation pressure and p_0 the atmospheric pressure) is equal to 6·0, giving a shock Mach number $M_s = 1{\cdot}69$ at the nozzle exit plane and a static pressure ratio across the shock of 3·165.

A value of $b = 0{\cdot}3$ was used for the adjustable constant in calculating the artificial viscosity. This value was selected after examining the effect of two other values of the constant, $b = 0$ and $b = 0{\cdot}5$, equation (5), on the computed pressure distribution along the axis of symmetry, as shown in figure 2.

The variables have been non-dimensionalized by using atmospheric conditions and the nozzle diameter as reference quantities, as appropriate. Non-dimensional time is expressed as $\tau = a_0 t/d$, where t is the time elapsed from the instant when sonic conditions are applied at the nozzle exit. The development of the flow which is initiated by application of sonic conditions at the nozzle exit may be divided into two phases: a first

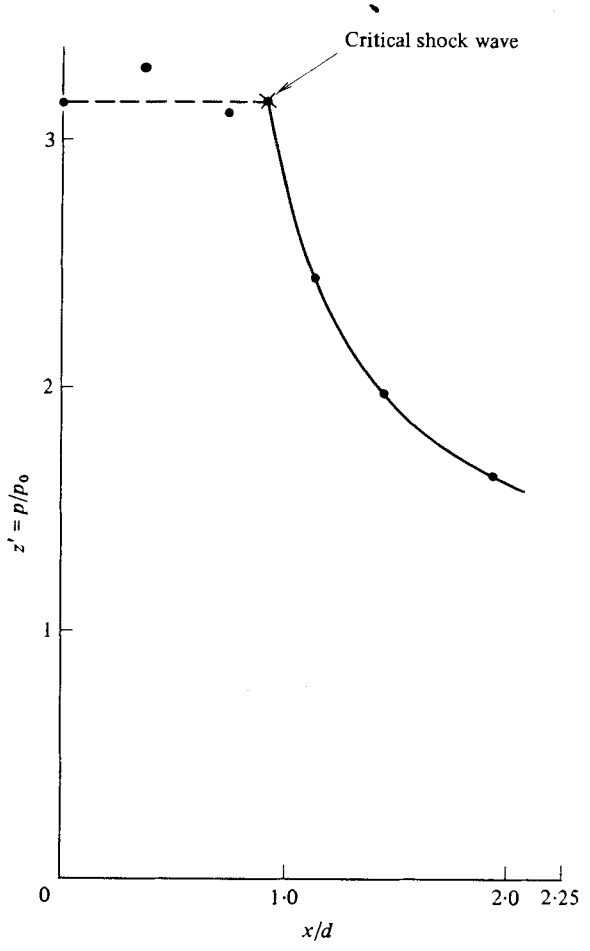

FIGURE 4. Decaying pressure behind critical shock wave on axis. – – –, initial shock-wave strength; ●, calculated results; -●-, results obtained by interpolation of experimental data (Sloan & Nettleton 1975).

phase during which the normal shock wave formed at the nozzle exit ($M_s = 1{\cdot}69$) reaches the plate, expanding in the process and becoming almost spherical; and a second phase during which this nearly spherical shock wave is reflected at the plate, the 'stand-off' shock wave is formed and begins to oscillate.

4.1. *Formation of spherical shock*

In figure 3 contours of pressure at times $\tau = 0{\cdot}446$ and $\tau = 0{\cdot}664$ are shown and the changes which take place as the shock wave moves downstream are clearly seen. The shock front, which is initially plane and perpendicular to the axis of symmetry, becomes curved as time progresses. It is evident in figure 3(*a*) ($\tau = 0{\cdot}446$) that the rarefaction wave originating at the rim of the nozzle has moved some way into the shocked gas and changed the shape of the shock front, except for that segment at the axis which is still plane. In figure 3(*b*) ($\tau = 0{\cdot}664$), however, it is seen that the entire shock front has been affected by the rarefaction wave and that it is now spherical over the greater portion of its surface, the centre of the radius of curvature being at the intersection of the axis of

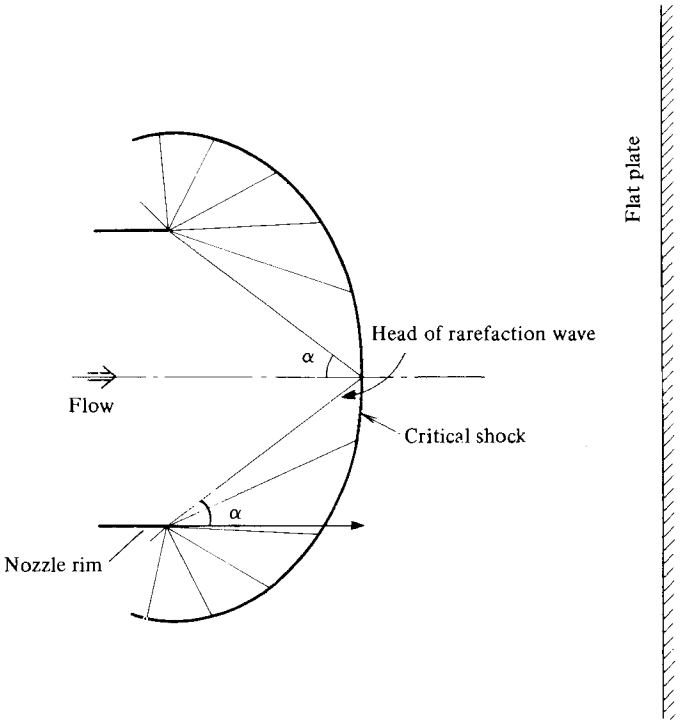

FIGURE 5. Diffracting initial shock wave: the critical shock.

symmetry with the nozzle exit plane. The centre of the expanding shock front remains in this position even when the shock wave reaches the plate at approximately $\tau = 1{\cdot}6$. This observation is at variance with the experimental results of Sloan & Nettleton (1975) which indicate that for an initial shock wave of the same strength ($M_s = 1{\cdot}69$) the centre of the spherical shock front would be located at about 0·6 nozzle diameters downstream of the exit plane.

Figure 4 shows the variation of the pressure ratio of the initial shock wave on the axis as it moves towards the plate. The dashed line is the pressure ratio of the initial shock wave of constant strength, equal to 3·165, which intersects the curve which has been drawn smoothly through the calculated points of decaying shock pressure ratio. The point of intersection demarcates the position x/d on the axis where the initial shock wave first begins to be affected by the rarefaction wave. It is the position of the 'critical shock wave' (Sloan & Nettleton 1975). Beyond this point the strength of the shock wave decays at the axis as the wave moves further downstream. The calculated strengths of the decaying shock wave, shown by the points in figure 4, are in good agreement with the experimental results of Sloan & Nettleton (1975). The curve drawn through the calculated points coincides with that obtained by interpolating their results for two shock waves of initial strengths $M_s = 1{\cdot}55$ and $M_s = 1{\cdot}92$.

Referring to figure 5, the angle α made by the head of the rarefaction wave with the flow direction at the critical shock position is given by (Skews 1967)

$$\tan^2\alpha = (\gamma-1)(M_s^2-1)\left(M_s^2+\frac{2}{\gamma-1}\right)\Big/(\gamma-1)M_s^4,$$

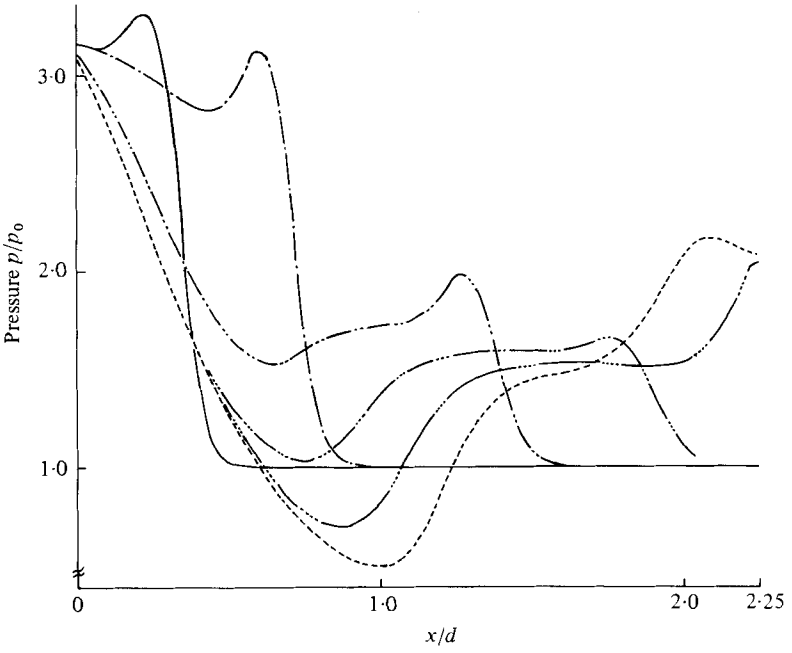

FIGURE 6. Pressure distribution along axis before merging of shock waves. ——, $\tau = 0{\cdot}222$; –·–, $\tau = 0{\cdot}446$; –··–, $\tau = 0{\cdot}863$; –···–, $\tau = 1{\cdot}249$; –····–, $\tau = 1{\cdot}601$; – – – –, $\tau = 1{\cdot}924$.

where M_s is the Mach number of the initial shock wave. For $M_s = 1{\cdot}69$, which is the initial shock strength in the present study, the calculated value of α is 28·6° which agrees closely with Skews' (1967) experimental curve.

Changes in pressure distribution along the axis at increasing times are shown in figure 6. After time $\tau = 0{\cdot}446$ the shock wave decays quickly. It may be noted that at $\tau = 0{\cdot}863$ a second shock wave is beginning to form in the expansion region behind the initial shock wave. The initial shock wave decays continuously due to the fact that rarefaction waves always catch up with the shock front from behind. These waves are reflected from the shock front as compression waves but since the flow behind the initial shock is supersonic the reflected waves cannot propagate upstream and therefore coalesce to form a second shock which is swept downstream. This shock becomes stronger as the reflected compression waves overtake it one after another. The half-space pressure distribution on a radial plane containing the axis of symmetry is shown in figure 7 for $\tau = 1{\cdot}601$. The pressures shown are the calculated values at cell centres which are 0·25 mm ($\frac{1}{2}\Delta r$) above the axis of symmetry, the boundary cells being at 0·25 mm ($\frac{1}{2}\Delta x$) from the nozzle exit plane. On the axis itself the pressure is higher and at the plane of the nozzle exit the value of p/p_0 is 3·17, as in figure 6.

4.2. *Reflection of primary shock from plate*

At approximately $\tau = 1{\cdot}6$ the initial shock wave, which is by now spherical, arrives at the flat plate on the axis. After reflection there, the pressure on the plate increases, attains a maximum at $\tau = 3{\cdot}683$ and thereafter decreases gradually. The variation of pressure on the plate is shown in figure 8.

The reflected initial shock wave propagates upstream and the half-space pressure

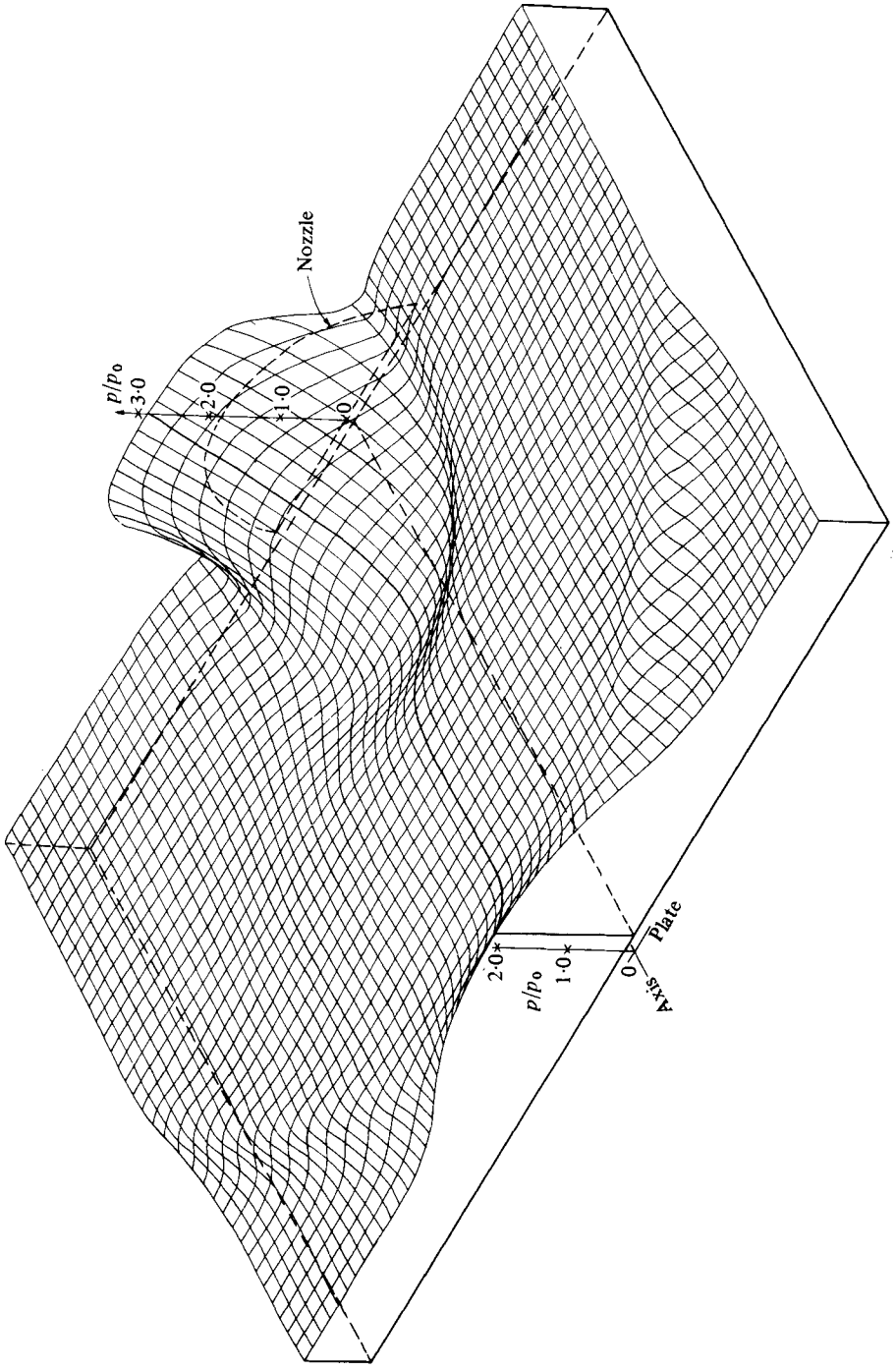

FIGURE 7. Pressure distribution in half-space at $\tau = 1{\cdot}601$ showing early stages of shock reflection and formation of second shock wave.

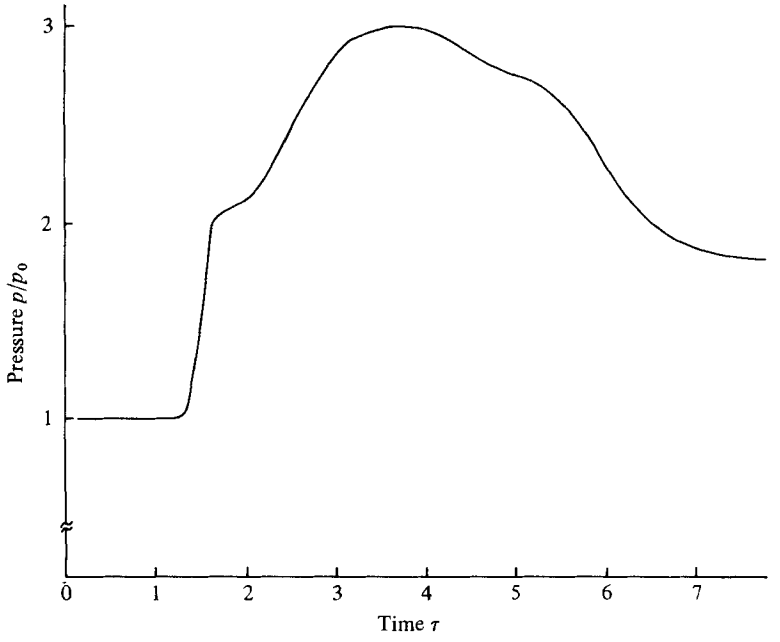

FIGURE 8. Variation of pressure on plate at axis.

distribution on a radial plane containing the axis of symmetry is shown in figure 9 for $\tau = 2{\cdot}228$. As in figure 7 the distribution has been calculated at cell centres so that on the axis itself the pressures will be somewhat greater. The relative positions and pressure amplitudes of the reflected initial shock wave and the second shock wave may be seen in figure 7.

On the axis, changes in pressure ratio after the reflected shock wave and the second shock wave first begin to merge at $\tau = 2{\cdot}665$ are shown for different times in figure 10. Merging of the two shock waves results in a strong shock which continues to propagate upstream into the supersonic jet flow but after time $\tau = 6{\cdot}303$ it begins to weaken and is swept downstream. Comparison of figure 10 with figure 6 shows that in the region of expansion between the nozzle exit and a radial plane located at approximately $x/d = 1{\cdot}0$, near-steady conditions have been attained at $\tau = 1{\cdot}924$ and that after this time the flow pattern remains essentially unchanged.

4.3. *Vortex formed in the jet between the shock and the plate*

Immediately after the reflected initial shock wave and the second shock wave merge a small toroidal vortex is formed near the axis of symmetry in the region between the merged shock wave and the plate. Figure 11 is a plot at time $\tau = 3{\cdot}683$ of some streamlines, the merged shock wave, or 'stand off' shock wave, and two contact surfaces which have been drawn using the calculated data for the velocity vectors, for pressure and for changes of entropy. Although smearing by the differencing scheme makes it difficult to locate precisely the discontinuity, nevertheless the general features of the experimental flow pattern are well described. By this time ($\tau = 3{\cdot}683$) merging of the reflected initial shock wave with the second shock wave, which in figure 9 are seen approaching one another, has been completed and the contact surface is located to the

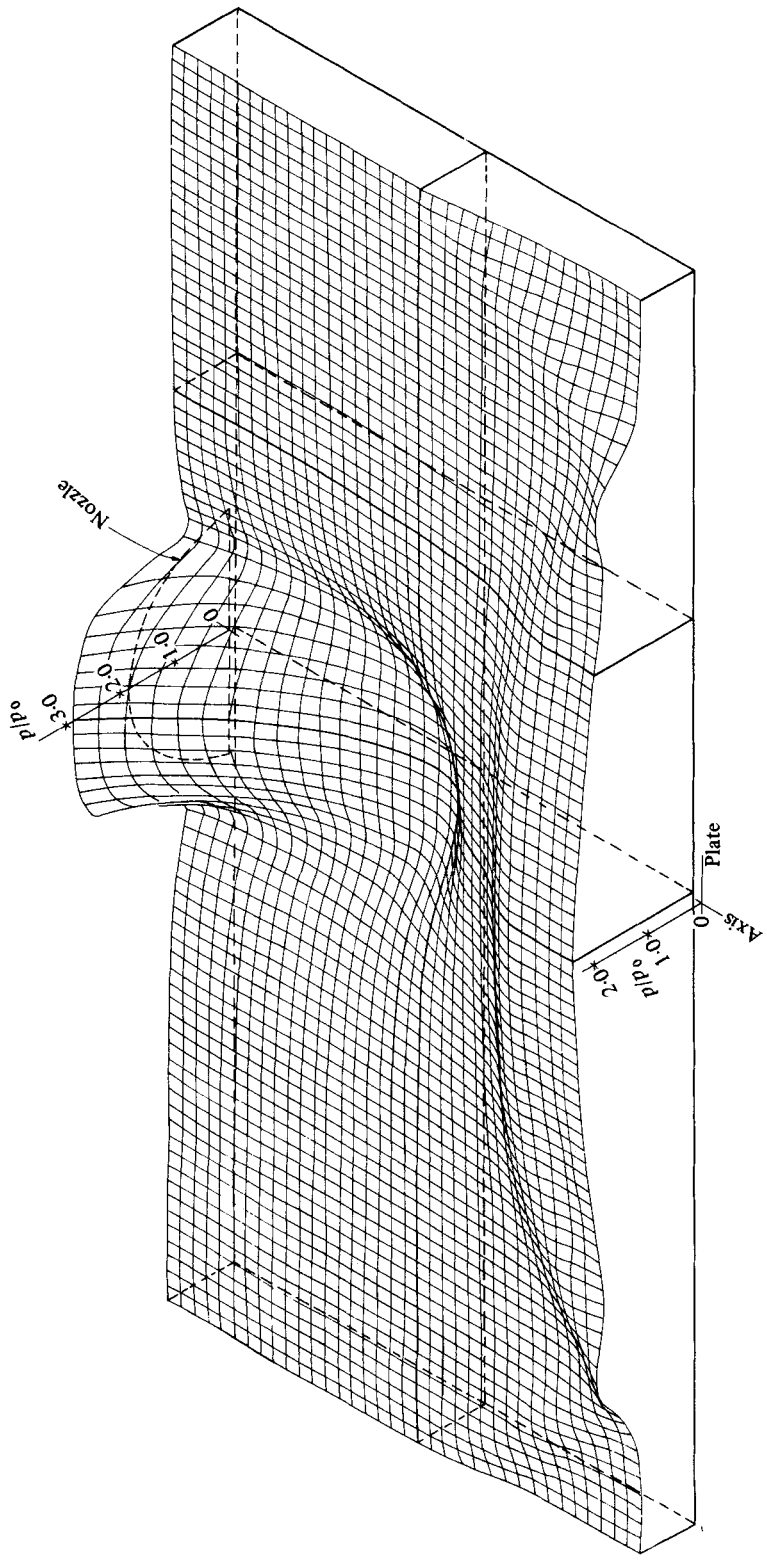

FIGURE 9. Pressure distribution on half-space at $\tau = 2{\cdot}228$ showing reflected shock wave and second shock wave about to merge.

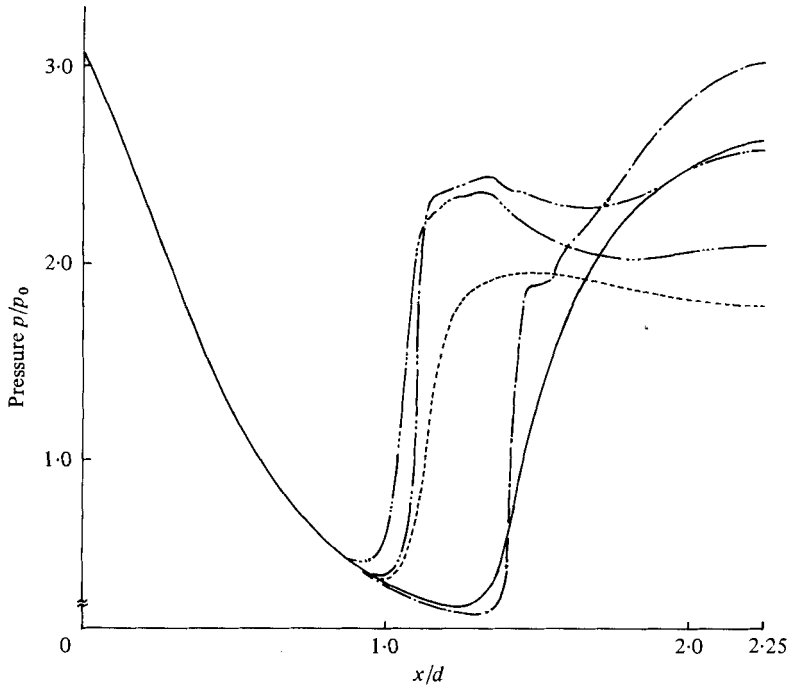

FIGURE 10. Pressure distribution on axis after merging of shock waves has commenced. ——, $\tau = 2{\cdot}665$; –·–, $\tau = 3{\cdot}683$; –··–, $\tau = 5{\cdot}575$; ----, $\tau = 6{\cdot}303$; – – –, $\tau = 7{\cdot}758$.

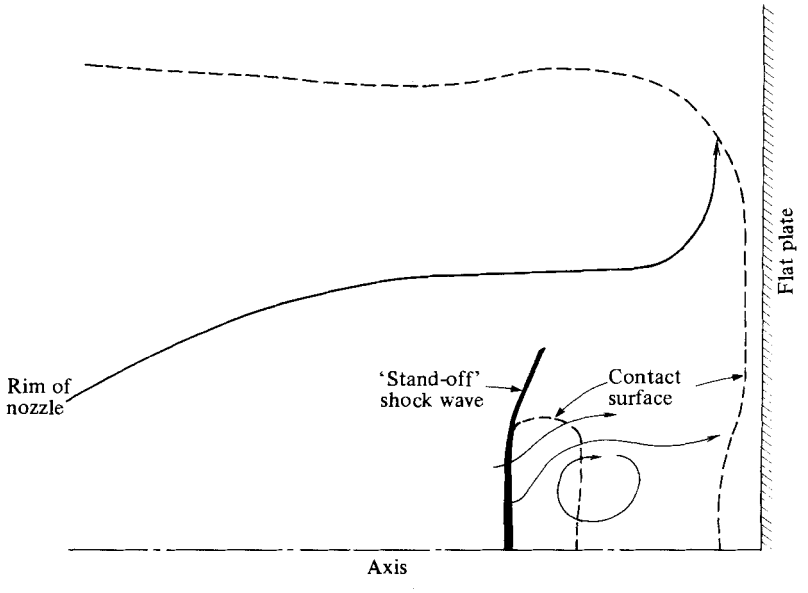

FIGURE 11. Flow field at $\tau = 3{\cdot}683$ – – –, contact surfaces. ——, streamlines; ——, shock wave.

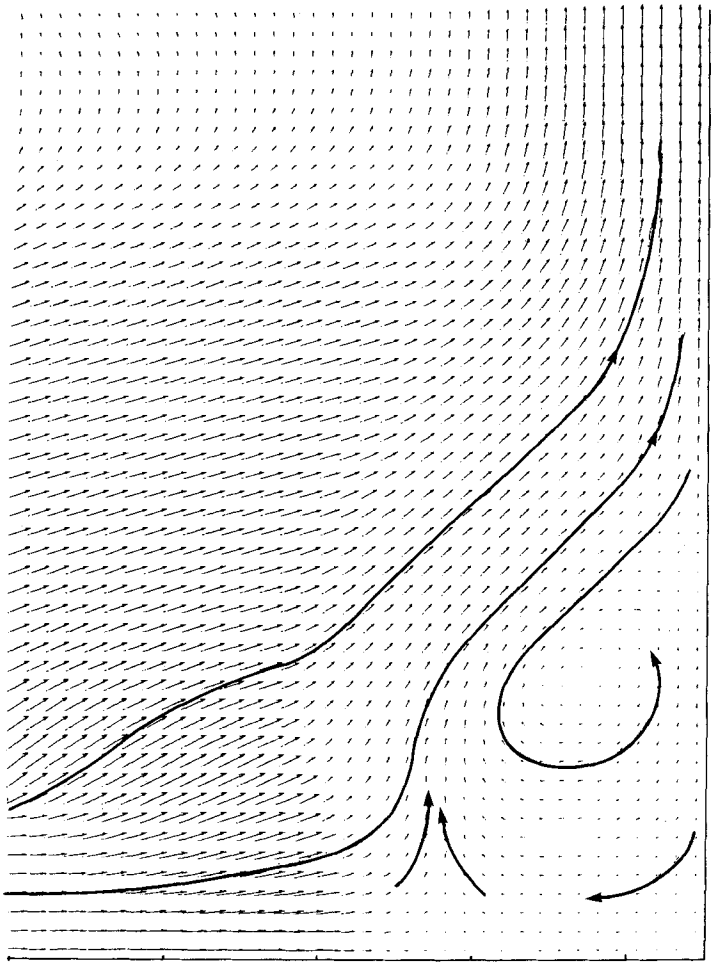

FIGURE 12. Velocity vector plot at $\tau = 7{\cdot}031$ with streamlines superimposed.

right of the merged shock wave and nearer to the plate. The extended contact surface shown is, in fact, the envelope of the farthest positions reached by fluid particles which were at the nozzle exit when sonic conditions were initially applied there. Merging of the reflected initial shock wave with the second shock wave, which begins at $\tau = 2{\cdot}665$, generates a rarefaction wave (Rudinger 1969) so that flow on the axis between the merged shock wave and plate is accelerated upstream and local flow reversal occurs. As successive points of superimposition move radially outward from the axis, they are accompanied by the continuous generation of rarefaction waves. Accordingly, flow reversal in the region between the merging shock waves and plate also spreads radially outward from the axis. The toroidal vortex which is formed when the flow first begins to reverse, grows as flow reversal spreads in the manner just described. A plot of velocity vectors at time $\tau = 7{\cdot}031$ is shown in figure 12. From a comparison with figure 11, it is evident that the toroidal vortex has moved further away from the axis of symmetry.

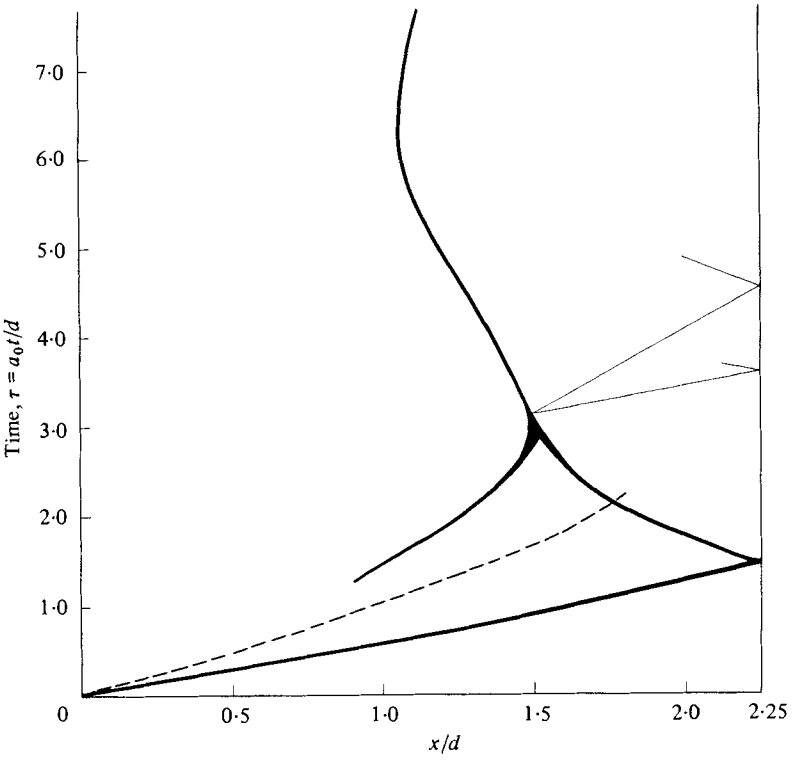

FIGURE 13. Wave diagram for flow at axis. – – –, contact surface; ——, rarefaction waves; —, shock wave.

4.4. *Wave diagram for flow on the axis*

Because of smearing it is difficult to obtain accurately positions of the shock wave and the contact surface. However, by taking average positions of the smeared discontinuities on the axis a wave diagram may be drawn as in figure 13. The shock wave initially at the nozzle exit propagates downstream with slightly decreasing velocity as it expands and reaches the plate at approximately $\tau = 1{\cdot}6$. Meanwhile, the second shock wave forms behind the primary shock at the approximate position $x/d = 0{\cdot}9$ and moves downstream. This shock wave is actually left-running but because the flow upstream is supersonic it cannot propagate in that direction and consequently is swept downstream and merges with the reflected initial shock wave. It is not a collision and merging produces a single strong shock wave, the process being accompanied by the continuous generation of rarefaction waves at successive points of superimposition.

The head of this rarefaction wave arrives at the plate at an approximate time $\tau = 3{\cdot}683$. It is difficult to define this time precisely because of smearing by the differencing scheme but its arrival signals the onset of decay of the pressure behind the reflected shock wave (figure 8).

The merged shock wave moves upstream in the jet at nearly constant velocity until $\tau = 6{\cdot}303$, which is also reflected in the pressure distribution shown in figure 10. At this instant it is at a minimum distance from the nozzle and thereafter begins to move downstream. The minimum distance of approach of the merged shock wave to the nozzle

corresponds to that position when the tail of the rarefaction wave reflected from the plate just reaches the shock which is still moving upstream. The arrival of the reflected rarefaction wave weakens the merged shock wave which now begins to move downstream towards the plate. Also, at about this time the reversed flow at the axis begins to decrease and its velocity becomes nearly zero at time $\tau = 7{\cdot}758$. At this instant the torroidal vortex is located at a radial distance from the axis of 1·5 nozzle diameters.

5. Conclusions

Using the computational scheme known as the fluid-in-cell method, the structure of the flow field in the early phase of impingement of an axisymmetrical underexpanded sonic jet on a flat plate has been obtained.

No experimental data are available for comparison with this phase of the development of the flow field but certain features which appear in flow-visualization studies under stable conditions are well reproduced. The results of the computer simulation indicate clearly how certain features which have been observed experimentally (Kukita 1975) arise in the flow field, such as the oscillation of the 'stand-off' shock wave, the periodic appearance of two contact surfaces and the growth and decay of the toroidal vortex. Where quantitative evaluation of the results is possible, agreement with experiment (Sloan & Nettleton 1975; Skews 1967) is good; for example, the attenuation of the expanding primary shock wave and the angle made by the head of the rarefaction wave at the position of the critical shock.

The authors are of the opinion that, because of very difficult experimental problems associated with measurements due to the limitation of the physical size of the experiment and to the nature of the flow, computer simulation is at present the only viable method of obtaining the quantitative and qualitative data concerning the processes leading to the stable resonant conditions that have been observed.

REFERENCES

Deckker, B. E. L. & Yang, A. 1975 *Proc. Inst. Mech. Eng.* **189**, 293.

Deckker, B. E. L. 1979 *Intern. J. Mech. Sci.* **21**, 41.

Donaldson, C. D. & Snedeker, R. S. 1971 *J. Fluid Mech.* **45**, 281.

Gentry, R. A., Martin, R. E. & Daly, B. J. 1966 *J. Comp. Phys.* **1**, 87.

Hartmann, J. 1931 *Phil. Mag.* **11**, 926.

Henderson, L. F. 1966 *Z. angew. Math. Phys.* **17**, 553.

Iwamoto, J. & Deckker, B. E. L. 1979 *Proc.* 7th Canadian Congress of Applied Mechanics, p. 585.

Kukita, T. 1975 Preprint of Japan Soc. of Mech. Engrs, 750–16, 229.

Moerch, K. 1964 *J. Fluid Mech.* **20**, 141.

Rudinger, G. 1969 *Nonsteady Duct Flow.* Dover.

Sloan, S. A. & Nettleton, M. A. 1975 *J. Fluid Mech.* **71**, 769.

Skews, B. W. 1967 *J. Fluid Mech.* **29**, 297.

Thompson, P. A. 1964 *A.I.A.A. J.* **2**, 1230.